Original article

Pristine and palladium-doped perovskite bismuth ferrites and their nitrogen dioxide gas sensor studies

Shivaji D. Waghmare [a,b], Siddheshwar D. Raut [b], Balaji G. Ghule [b], Vijaykumar V. Jadhav [c], Shoyebmohamad F. Shaikh [d,*], Abdullah M. Al-Enizi [d], Mohd Ubaidullah [d], Ayman Nafady [d], Badr M. Thamer [d], Rajaram S. Mane [b,*]

[a] Department of Physics, Shri. Shivaji Mahavidyalaya, Barshi, Solapur, India
[b] School of Physical Sciences, S. R. T. M. University, Nanded 431606, M.S., India
[c] Department of Physics, Shivaji Mahavidyalaya, Udgir, Latur, India
[d] Department of Chemistry, College of Science, King Saud University, Riyadh 11451, Saudi Arabia

ABSTRACT

Undoped and palladium-doped perovskite bismuth ferrite nitrogen dioxide (NO_2) gas sensors (BiFeO₃ i.e. BFO and Pd-BiFeO₃ i.e. Pd-BFO) are successfully synthesized *via* an easy and low-cost sol–gel process. The Pd-doping in BFO is confirmed through an X-ray diffraction data, field emission scanning electron microscopy images, energy-dispersive X-ray spectroscopy analysis, and its influence on the structure, morphology, surface area, and the NO_2 gas sensor performance of the BFO sensor has been examined and explored. Moreover, the plausible gas sensing response mechanism of Pd-BFO film sensor has also been proposed. The nanocubes embedded into a uniformly distributed upright standing nanoplates facilitate better gas adsorption and diffusion behavior on providing an excellent NO_2-sensing performance with good sensitivity, excellent selectivity, better response (90 s)/recovery (110 s), and noticeable repeatability under a fixed 100 ppm NO_2 gas concentration level at an optimized low operating temperature i.e. 150 °C.
© 2020 The Author(s). Published by Elsevier B.V. on behalf of King Saud University. This is an open access article under the CC BY-NC-ND license (http://creativecommons.org/licenses/by-nc-nd/4.0/).

1. Introduction

Nitrogen dioxide (NO_2), as one of the important sources for air pollutant, has attracted a considerable attention due to its adverse impact on human life and environmental concerns (Liu et al., 2019) (Liu et al., 2019) (Liu et al., 2019) (Liu et al., 2019). On ground level, 15 ppb of NO_2 gives rise to irritation of eyes, nose and throat; for middle 30 ppb, people can be infected by airway hyperactivity of muscles; and upper 80 ppb level, the respiratory tract infections are drastically increased (Liu et al., 2016). Detection of toxic and hazardous gases at an early stage is major concern. Therefore, there is an urgent need to develop a new class materials of high-performance gas sensors to detect the NO_2 gas in an economic

way. In last few years, ternary metal oxides based on perovskite ABO_3 type structures demonstrated steadfast gas-sensing properties and performance compared to other binary oxides, which could be due to different analytes ranging from cations and their capability to accept various doping elements (George K et al., 2020). Ferrites with various perovskite-based structures i.e. BiFeO₃, LaFeO₃, PrFeO₃, EuFeO₃, GdFeO₃, have demonstrated different degrees of gas sensor performance (Niu et al., 2004; Siemons et al., 2007).

Recently, various metal dopants in perovskite-based ferrite structures are used to enhance their gas sensing response and selectivity towards various gases. Fan et al. reported that the Ba-substituted BFO sensor increased gas-sensing performance due to presence of a large concentration of oxygen vacancy as compared to pure BFO (Dong et al., 2015). Mane et al. reported a high performance of tungsten-doped BFO nano sensor over pristine for NO_2 gas (Waghmare et al., 2018). Pal et al. approved 25 s response/17 s recovery time at low concentration of acetone vapors for BFO nanoparticle-sensors (Chakraborty and Pal, 2019). Mursalin et al. reported sono-chemically synthesis of BFO nanoparticle sensors with an outstanding SO_2 gas sensing performance and ultrafast response/recovery time (Das et al., 2015). Pal et al. prepared BFO

gas sensors that endowed a fast response (25 s)/recovery time (13 s) for carbon monoxide gas which is fixed to 30 ppm level (Chakraborty and Pal, 2018).

A perovskite bismuth ferrite (BFO) has been fascinated impressive considerations because of its special and unique properties including a high Curie temperature ($T_C \sim 1100$ K) and Neel temperature ($T_N \sim 643$ K) (Wang et al., 2003; Zhang et al., 2007). Moreover, BFO film plays a vital role due to its large spontaneous polarization (90–100 $\mu C/cm^2$) and piezoelectric response (~70 pm/V), which are essentially important in gas sensor and micro-electromechanical devices (Chu et al., 2006; Martin et al., 2010). Various approaches are being adopted to obtain BFO nanostructures of various morphologies such as nanoparticles (0 D) (Soltani and Entezari, 2013), nanorods, nanoflask, and nanotubes (1 D) (Wang et al., 2009), nanodisks, nanosheets, and nanorings (2D) (Luo et al., 2017), urchin-like and dendrites (3 D) etc., (Kozeeva et al., 2011) with surface areas for improving gas sensing performance that can provide a large contacting interfacial area between the gas sensors and target gases. Until now, several physical and chemical synthesis processes such as magnetron sputtering (Deng et al., 2016), solvothermal process (Liu et al., 2014), hydrothermal (Rouhani et al., 2019), microwave (Azeem et al., 2019), and wet chemical method (Sakar et al., 2013) etc., were envisaged to obtain BFO in different structures and morphologies. Said synthesis processed needed either costly instruments or multiple complicated chemical time consuming steps with harmful waste. In wet chemical method, very less amount of material deposited on the film surface, is essentially required relatively high reaction temperature which hinders for a large scale production potential. In electrodeposition method, large-scale uniform deposition of material on conducting substrate is a big problem. Whereas, in spray pyrolysis method, production of hazardous and toxic bi-products are generally ignored. Among these, due to eco-friendly and easy scalability, sol–gel chemical synthesis method can be used for the synthesis of BFO with controlled shapes and sizes.

In present study, BFO and Pd-BFO nanostructures were synthesized *via a* sol–gel chemical synthesis process for the production of ultra-fine nanostructures with high surface-to-volume ratio. The effect of Pd-doping on the structure surface morphology evolution, surface area, and NO_2 gas sensing performance of pristine BFO was investigated. Moreover, the plausible gas sensing response mechanism of Pd-BFO nanostructured film sensor has also been discussed. In Table 1 review data of the as-synthesized BFO-based gas sensors are provided.

2. Results and discussion

2.1. Structure elucidation and morphology evolution studies

The XRD analysis is one of the most important characterization methods to study the crystal structures of metallic, semiconducting and amorphous materials. As-obtained prominent XRD peaks of BFO were indexed to rhombohedral *R3c* space group of per-

ovskites $BiFeO_3$. In Fig. 1(a), strongly assigned lattice planes of (101), (012/110), (003), (202), (113), (104), (300), (024), (220), (015), (303), and (312), that are closely matching to reported data for BFO i.e. $BiFeO_3$ [JCPDS card no.20–0169] (Liu et al., 2005) were identified. In Pd-BFO XRD pattern, the intense peak was (021/111) at near 40° and two other peaks indexed to (*) were newly appeared with very low intensity, indicating existence of Pd with BFO. The average particle size of Pd-BFO calculated using Debye-Scherrer method was 5 nm. The peak of diffractogram corresponding to maximum intensity at 31.82° (2θ) for 2.81 Å *d*-value was due to BFO. The EDX spectrum as shown in Fig. 1b demonstrated Bi, Fe, O and Pd elements, suggesting an incorporation of Pd in BFO. There were no any other phase or impurities present in the sample suggesting synthesis of defect free Pd-BFO film.

The surface morphologies, scanned at different magnifications, of the BFO and Pd-BFO film sensors are exhibited in Fig. 2 (a-d) where both BFO and Pd-BFO demonstrated dual architectures i.e. nanocubes and nanoplates. In a wide FE-SEM image, nanocube-type morphology was inter-connected to spongy-type nanoplates. As compared with nanoplates, the density of nanocubes was limited. We believed that this dual surface morphology (plates and cubes) of higher surface area could be helpful for gas sensing applications. The high-resolution images endowed the nanocubes of equal dimensions embedded into uniformly distributed and vertical aligned nanoplates. In surface morphology, we observed that the nanocubes were partially incorporated in nanoplate surfaces with enhanced interconnectivity. Noticeably, nanoplate structure was growth in 1D direction, whereas nanocubes were in 3D. The as-obtained dual morphology sensor could afford a large surface-to-volume ratio for an easy gas molecules percolation to obtain a better gas sensing performance (Liu et al., 2005). The surface morphologies of Pd-BFO film are shown in Fig. 2c and d. In Pd-BFO film sensor, side surfaces of nanocubes were relatively rough as compared to pristine BFO film sensor. The formation of smaller Pd-nanoparticles as seen onto Pd-BFO surface could provide an additional benefits. As noted extensive voids and spaces between both morphologies could have allowed easy, fast and deep percolation of gas molecules (Zhang et al., 2015).

2.2. Surface area and pore-size distribution estimations

The N_2 adsorption–desorption isotherms of pristine BFO and Pd-BFO are presented in Fig. 3(a, b) that demonstrated type IV isotherms with H_4 hysteresis-type, evidencing an involvement of mesopores nature (Khan et al., 2018; Thommes, 2010). Moreover, in the middle part of the isotherm, the lower slope could be attributed to the multilayer adsorption. The specific surface areas for BFO and Pd-BFO were respectively 4.37, and 12.22 $m^2 \cdot g^{-1}$, suggesting enhancement of BFO surface area on Pd doping which could be attributed to a change of the surface morphology. The insets of Fig. 3(a, b) confirm pore-diameter plots of BFO and Pd-BFO sensors where pore-size was centered to ~10 nm in accord

Table 1
A review data on BFO-based gas sensor studies.

Material	C (ppm)	S (%)	T (°C)	τ_{res}	τ_{rec}	Ref.
$BiFeO_3$	200	6.6	240	20	14	(Zhu et al., 2019)
$BiFeO_3$	50	40	260	2	2	(Yu et al., 2009)
$ABFO_4$	10	72.62	240	13	24	(Li et al., 2018)
$Bi_{0.9}Ba_{0.1}FeO_{2.95}$	100	14	400	3	10	(Dong et al., 2015)
BiFeO3	10	12	350	25	17	(Chakraborty and Pal, 2019)
BiFeO3	50	30	240	5	8	(Zhang et al., 2018)
BiFeO3	30	2.12	250	25	13	(Chakraborty and Pal, 2018)
$Pd-BiFeO_3$	100	75	140	60	100	Current work
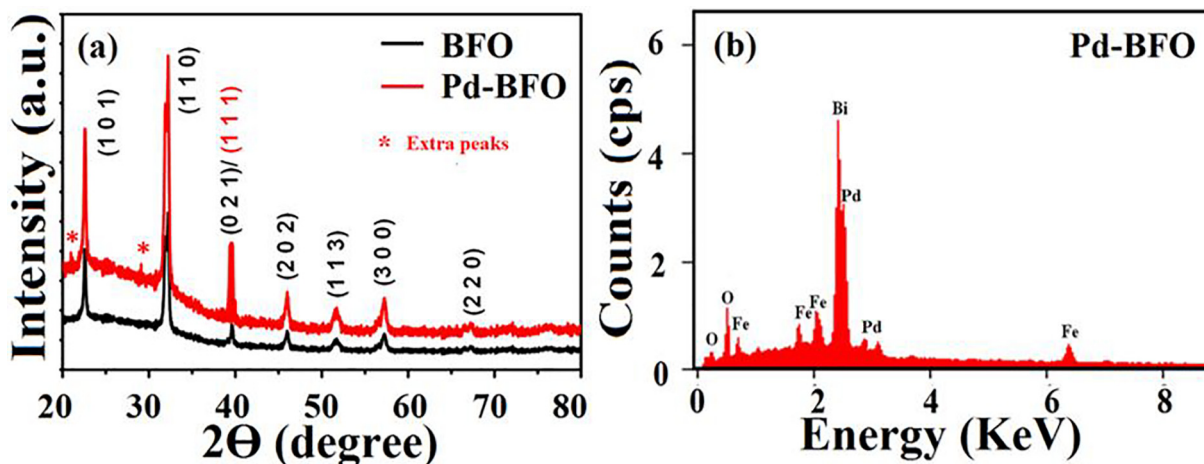
Fig. 1. a) XRD patterns of pristine BFO and Pd-BFO thick film sensor and, b) EDAX analysis over Pd-BFO film sensor surface.
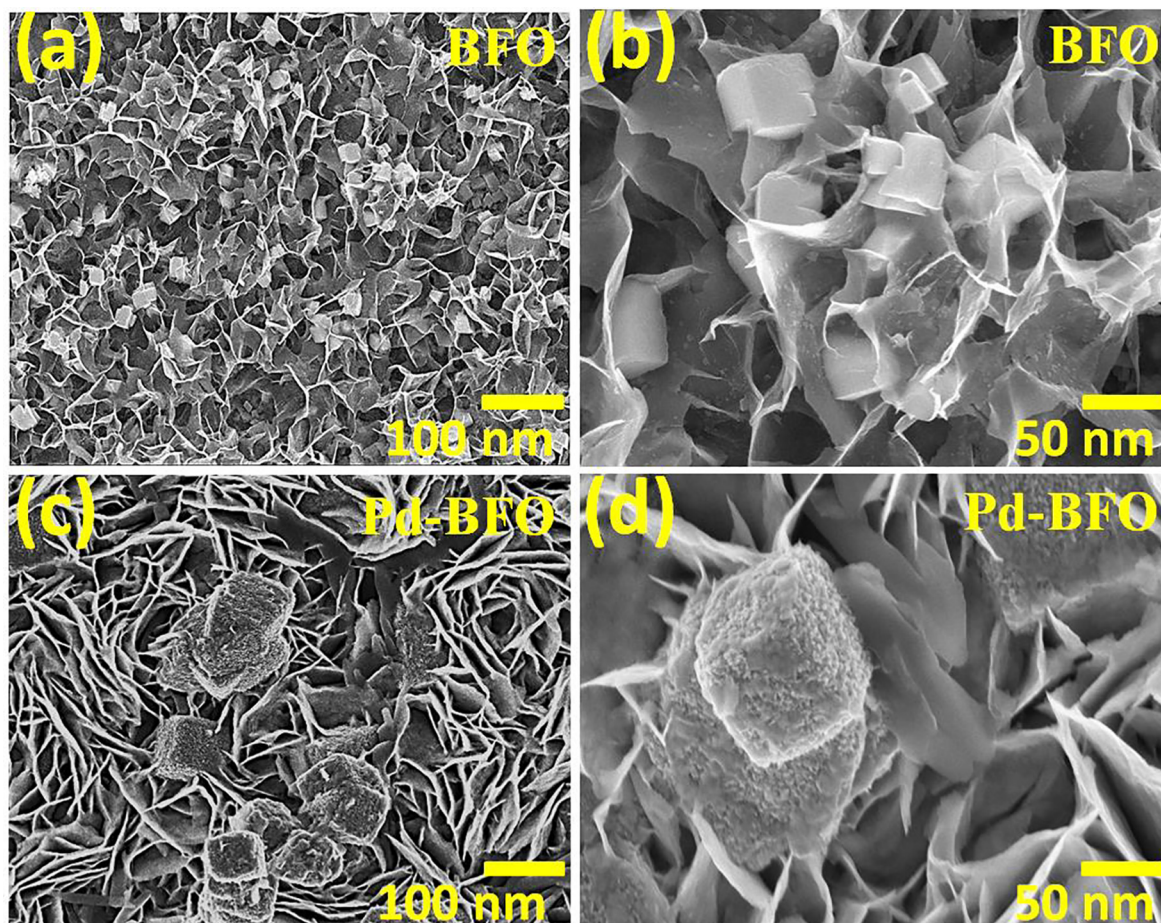
Fig. 2. FE-SEM images of; (a, b) pristine BFO, and (b, c) Pd-BFO film sensors at two magnifications.

to their mesoporous character, suggesting that on Pd doping the pore-size of BFO sensor was not endowed a significant change.

2.3. Gas sensor properties

The NO$_2$ gas sensing performances of BFO and Pd-BFO film sensors are demonstrated in Fig. 4 (a-d). Fig. 4(a) demonstrates the responses of the BFO and Pd-BFO sensors for NO$_2$ gas at various operating temperature range. The maximum gas sensing responses of both BFO and Pd-BFO sensors were optimized at 150 °C operating temperatures at a fixed 100 ppm concentration level of NO$_2$ gas. The gas sensitivity decreased with increase of the operating temperature from 150 to 250 °C, suggesting operating temperature has very significant impact on NO$_2$ gas sensor performance. In particularly, with change in the operating temperature, the adsorption/desorption kinetics and chemical reactions taking place over
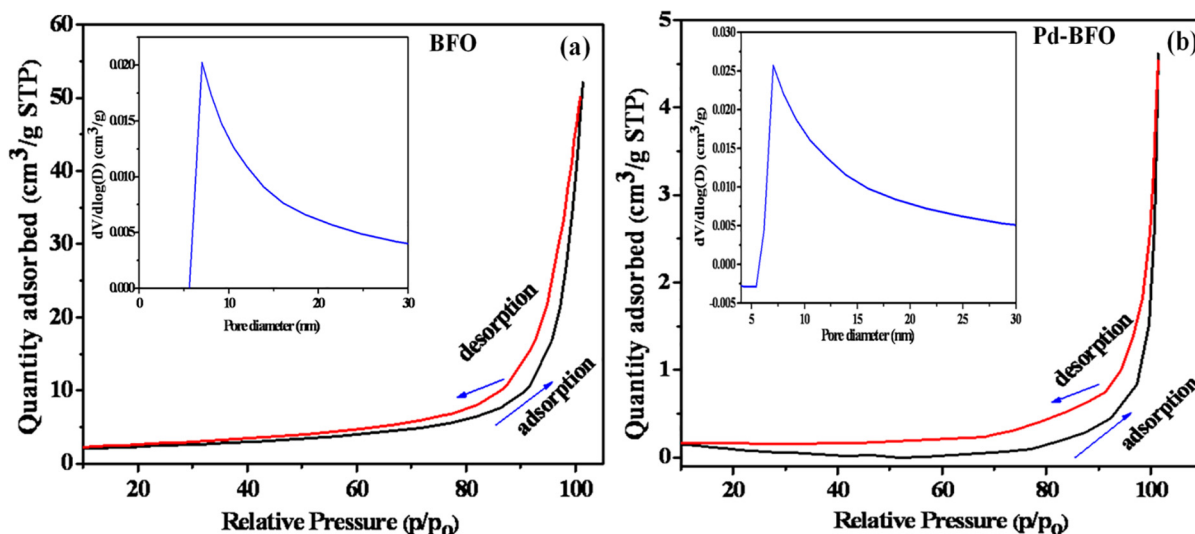
Fig. 3. N$_2$ adsorption–desorption isotherms and corresponding pore-size distribution curves (insets) of; a) pristine BFO, and b) Pd-BFO sensors.
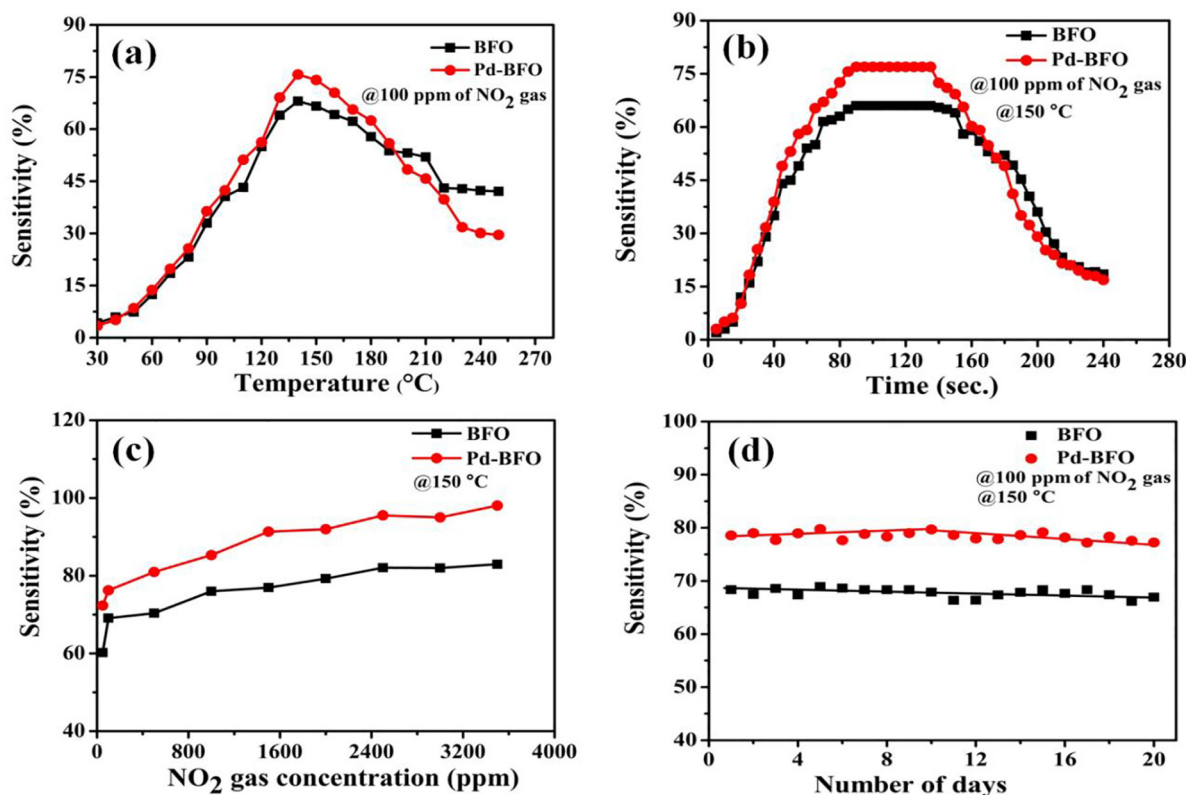
Fig. 4. a) The NO$_2$ sensitivity of BFO and Pd-BFO sensors at 100 ppm, b) response/recovery curves of the sensors recorded at fixed 100 ppm NO$_2$ gas and optimal temperature (150 °C), c) The NO$_2$ sensitivity of the films at optimal temperature with various NO$_2$ gas concentrations (50–3500 ppm), and (d) the stability testing curve of the films.

sensor surface of gas sensor were altered, leading to produce variation in sensor sensitivity. When operating temperature further enhanced to a certain temperature, the desorption rate of the gas increased, resulting in decrease of the total quantity of adsorbed gas molecules (Barsan et al., 1999). Response time is the time essential for sensor to reach the maximum steady state value of its sensitivity in the exitance of gas. Whereas, recovery time is defined as the time required for the sensor to reach an ideal steady state value after the target gas was taken out. On the basis of the gas sensor performance, the response (t$_{res}$)/ recovery (t$_{rec}$) time

values of the BFO and Pd-BFO were obtained i.e. 150 °C at optimized operating temperature for 100 ppm of NO$_2$ target gas which is shown in Fig. 4b. The sensor recovery was estimated by exposing the sensor chamber to the external atmospheric air. The obtained response/recovery time for Pd-BFO was 90/110 s which is similar to BFO sensor and could be attributed to equal pore size distribution of both the sensor materials (Almar et al., 2015). The NO$_2$ response values of the BFO and Pd-BFO sensors at various concentrations were noted and are shown in Fig. 4(c). The lowest NO$_2$ concentration detection level, with a 75% response, was

100 ppm. The NO₂ responses of the BFO and Pd-BFO sensors were increased with the gas concentration until the sensor surfaces could completely cover the adsorbed target NO₂ molecules. The maximum NO₂ response at a concentration of 3600 ppm was 93%. The dynamic repeatability tests of the BFO and Pd-BFO sensors tested for NO₂ gas at 100 ppm concentration are shown in Fig. 4(d). The repeatability of the sensor was compatible. The stability tests of the BFO and Pd-BFO sensors for NO₂, as shown in Fig. 4(d) were nearly constat for 20 days, confirming the chemical stability and mechanical robustness. The comprehensive review of the previous reports is provided in Table 1.

2.4. NO₂ gas sensing mechanism

The mechanism of gas sensor consists of change in the resistance on the sensor material surface depending on the adsorption–desorption processes of gas molecules. On exposure of sensor surface to atmospheric air, as shown in Fig. 5a, the Pd-BFO sensor chemisorbs oxygen molecules and get converted into equivalent chemisorbed oxygen species (O_2^- and O^-) by acquiring electrons through the conduction band of sensor material, resulting in the creation of an electron-depleted space-charge layer on the sensor material surface which is shown in Eqs. (2)–(4). At different operating temperatures, the primary presence of oxygen species changes accordingly. When operating temperature is below 150 °C, oxygen species are existing in the form of O_2^- or O^-. The constant concentration of surface oxygen is understood by acquiring a constant electrical resistance in presence of atmospheric air. When NO₂ is injected in the sensing chamber, as demonstrated in Fig. 5b, the different chemisorbed oxygen ions on the material surface may interact with NO₂, and meantime, the electrons get adsorb by NO₂ from the conduction band due to its special electrophilic property to produce adsorbed NO₂ (ads)⁻, as demonstrated in Eqs. (5) and (6). This process reduces the concentration of electrons on the sensor material surface, thickens the depletion layer, with enhanced the potential barrier, resulting the incremet in the resistance of sensor material (Qi et al., 2015). The recovery of sensor can be achieved by opening the outlet of sensing chamber with introduction of fresh atmospheric air in the chamber, the plausible chemical reaction expressed in Eq. (7). The Pd-BFO-based gas sensor film demonstrated excellent response for NO₂, which could be due to one of its unique dual surface morphology equal dimensions nanocubes were embedded within uniformly distributed vertically aligned nanoplates, which offers abundant active surface sites and favorable conditions for NO₂ chemical adsorption, at the operating temperature of 150 °C. More-

over, dual surface morphology of different surface area may allow gas molecules simply to cover the sensing body for NO₂ diffusion. So, when exposed to an equal amount of NO₂ gas, more NO₂ will react with the various adsorbed oxygen ions (O_2^- and O^-) then causes the resistance of the sensor to enhance more quickly and noticeably compared to single surface morphology, thereby our gas sensor exhibited an excellent performance for detecting NO₂.

$$O_{2(gas)} \rightarrow O_{2(ads)} \tag{2}$$

$$O_{2(ads)} + e^- \rightarrow O_{2\ (ads)}^- \tag{3}$$

$$O_{2\ (ads)}^- + e^- \rightarrow 2O^-_{\ (ads)} \tag{4}$$

$$NO_{2(gas)} + e^- \rightarrow NO^-_{2(ads)} \tag{5}$$

$$NO_{2(gas)} + O_{2\ (ads)}^- + 2e^- \rightarrow NO^-_{2(ads)} + 2O^-_{\ (ads)} \tag{6}$$

$$NO^-_{2(ads)} + 2O^-_{\ (ads)} + e^- \rightarrow NO_{2(gas)} + 2O^{2-}_{2\ (ads)} \tag{7}$$
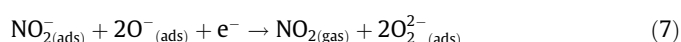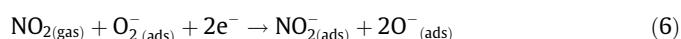
3. Conclusions

In summary, BFO and Pd-BFO film sensors are successfully synthesized *via* a simple and low-cost sol–gel chemical synthesis method. On FE-SEM study, both BFO and Pd-BFO demonstrated dual morphology i.e. a combination of nanocubes and nanoplates. The as-obtained dual morphology sensors facilitate a large surface area and abundant active sites which could be beneficial for easy gas molecules dicuss adsorption and diffusion processing. The as-synthesized dual morphology Pd-BFO-based gas sensor proves an excellent NO₂ gas sensing activity with high sensitivity, good selectivity, quite good response (90 s)/recovery (110 s), and remarkable 20 days repeatability to 100 ppm NO₂ concentration level at low operating temperature (~150 °C). These results demonstrated that the mesoporous Pd-BFO is a promising candidate for gas sensing applications and open up a new direction for using in commercial devices.

Declaration of Competing Interest

The authors declare that they have no known competing financial interests or personal relationships that could have appeared to influence the work reported in this paper.
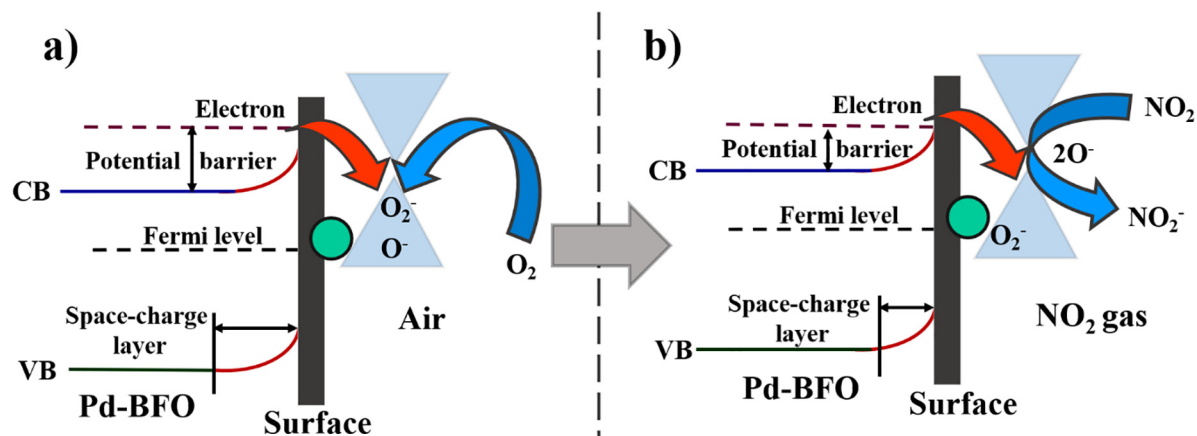
Fig. 5. Schematic diagram of the as-proposed response mechanism of our Pd-BFO film gas sensor to NO₂: (a) in air and (b) in the tested gas (CB: the bottom edge of conduction band, and VB: the topedge of valence band).

Acknowledgement

Appendix A. Supplementary data

Supplementary data to this article can be found online at https://doi.org/10.1016/j.jksus.2020.08.024.

References

Almar, L., Tarancón, A., Andreu, T., Torrell, M., Hu, Y., Dezanneau, G., Morata, A., 2015. Mesoporous ceramic oxides as humidity sensors: A case study for gadolinium-doped ceria. Sensors Actuators B Chem. 216, 41–48. https://doi.org/10.1016/j.snb.2015.04.018.

Azeem, W., Riaz, S., Bukhtiar, A., Sajjad Hussain, S., Xu, Y., Naseem, S., 2019. Ferromagnetic ordering and electromagnons in microwave synthesized BiFeO3 thin films. J. Magn. Magn. Mater. 475, 60–69. https://doi.org/10.1016/j.jmmm.2018.11.089.

Barsan, N., Schweizer-Berberich, M., Göpel, W., 1999. Fundamental and practical aspects in the design of nanoscaled SnO2 gas sensors: a status report. Fresenius. J. Anal. Chem. 365, 287–304. https://doi.org/10.1007/s002160051490.

Chakraborty, S., Pal, M., 2019. Highly selective and stable acetone sensor based on chemically prepared bismuth ferrite nanoparticles. J. Alloys Compd. 787, 1204–1211. https://doi.org/10.1016/j.jallcom.2019.02.153.

Chakraborty, S., Pal, M., 2018. Highly efficient novel carbon monoxide gas sensor based on bismuth ferrite nanoparticles for environmental monitoring. New J. Chem. 42, 7188–7196. https://doi.org/10.1039/C8NJ01237G.

Chu, Y.-H., Zhan, Q., Martin, L.W., Cruz, M.P., Yang, P.-L., Pabst, G.W., Zavaliche, F., Yang, S.-Y., Zhang, J.-X., Chen, L.-Q., Schlom, D.G., Lin, I.-N., Wu, T.-B., Ramesh, R., 2006. Nanoscale Domain Control in Multiferroic BiFeO3 Thin Films. Adv. Mater. 18 (17), 2307–2311.

Das, S., Rana, S., Mursalin, S.M., Rana, P., Sen, A., 2015. Sonochemically prepared nanosized BiFeO3 as novel SO2 sensor. Sensors Actuators B Chem. 218, 122–127. https://doi.org/10.1016/j.snb.2015.04.084.

Deng, X., Huang, J., Sun, Y., Liu, K., Gao, R., Cai, W., Fu, C., 2016. Effect of processing parameters on the structural, electrical and magnetic properties of BFO thin film synthesized via RF magnetron sputtering. J. Alloys Compd. 684, 510–515. https://doi.org/10.1016/j.jallcom.2016.05.114.

Dong, G., Fan, H., Tian, H., Fang, J., Li, Q., 2015. Gas-sensing and electrical properties of perovskite structure p-type barium-substituted bismuth ferrite. RSC Adv. 5, 29618–29623. https://doi.org/10.1039/C5RA01869B.

George, K.J., Halali, V.V., Sanjayan, C.G., Suvina, V., Sakar, M., Balakrishna, R.G., 2020. Perovskite nanomaterials as optical and electrochemical sensors. Chem. Front. Inorg. https://doi.org/10.1039/D0QI00306A.

Khan, H.A., Natarajan, P., Jung, K.-D., 2018. Stabilization of Pt at the inner wall of hollow spherical SiO2 generated from Pt/hollow spherical SiC for sulfuric acid decomposition. Appl. Catal. B Environ. 231, 151–160. https://doi.org/10.1016/j.apcatb.2018.03.013.

Kozeeva, L.P., Kameneva, M.Y., Podberezskaya, N.V., Smolentsev, A.I., Fedorov, V.E., 2011. Preparation and structural characterization of bismuth ferrite crystals of different morphological types. Inorg. Mater. 47 (1), 68–74. https://doi.org/10.1134/S0020168510121015.

Li, Q., Zhang, W., Wang, C., Ma, J., Ning, L., Fan, H., 2018. Ag modified bismuth ferrite nanospheres as a chlorine gas sensor. RSC Adv. 8, 33156–33163. https://doi.org/10.1039/C8RA06247A.

Liu, C., Henderson, B.H., Wang, D., Yang, X., Peng, Z., 2016. A land use regression application into assessing spatial variation of intra-urban fine particulate matter (PM2.5) and nitrogen dioxide (NO2) concentrations in City of Shanghai, China. Sci. Total Environ. 565, 607–615. https://doi.org/10.1016/j.scitotenv.2016.03.189.

Liu, X.-M., Fu, S.-Y., Huang, C.-J., 2005. Synthesis and magnetic characterization of novel CoFe2O4–BiFeO3 nanocomposites. Mater. Sci. Eng. B 121, 255–260. https://doi.org/10.1016/j.mseb.2005.04.009.

Liu, Y., Zuo, R., Qi, S., 2014. Surfactant-free solvothermal synthesis and optical characterization of Bi2Fe4O9 in mixed H2O/EtOH solvent. Powder Technol. 254, 30–35. https://doi.org/10.1016/j.powtec.2014.01.013.

Liu, Z., Guan, Q., Luo, H., Wang, N., Pan, N., Yang, L., Xiao, S., Lin, J., 2019. Development of land use regression model and health risk assessment for NO2 in different functional areas: A case study of Xi'an, China. Atmos. Environ. 213, 515–525. https://doi.org/10.1016/j.atmosenv.2019.06.044.

Luo, Q., Chen, D., Yang, W., Chen, C., Li, P., Huang, Z., Tian, G., Fan, Z., Gao, X., Liu, J.-M., 2017. Fabrication of epitaxial ferroelectric BiFeO3 nanoring structures by a two-step nano-patterning method. Ceram. Int. 43, 16136–16140. https://doi.org/10.1016/j.ceramint.2017.08.188.

Martin, L.W., Chu, Y.-H., Ramesh, R., 2010. Advances in the growth and characterization of magnetic, ferroelectric, and multiferroic oxide thin films. Mater. Sci. Eng. R Reports 68, 89–133. https://doi.org/10.1016/j.mser.2010.03.001.

Niu, X., Du, Weimin, Du, Weiping, 2004. Preparation, characterization and gas-sensing properties of rare earth mixed oxides. Sensors Actuators B Chem. 99, 399–404. https://doi.org/10.1016/j.snb.2003.12.006.

Qi, J.J., Gao, S., Chen, K., Yang, J., Zhao, H.W., Guo, L., Yang, S.H., 2015. Vertically aligned{,} double-sided{,} and self-supported 3D WO3 nanocolumn bundles for low-temperature gas sensing. J. Mater. Chem. A 3, 18019–18026. https://doi.org/10.1039/C5TA03711E.

Rouhani, Z., Karimi-Sabet, J., Mehdipourghazi, M., Hadi, A., Dastbaz, A., 2019. Response surface optimization of hydrothermal synthesis of Bismuth ferrite nanoparticles under supercritical water conditions: Application for photocatalytic degradation of Tetracycline. Environ. Nanotechnol., Monit. Manag. 11. https://doi.org/10.1016/j.enmm.2018.100198.

Sakar, M., Balakumar, S., Saravanan, P., Jaisankar, S.N., 2013. Annealing temperature mediated physical properties of bismuth ferrite (BiFeO3) nanostructures synthesized by a novel wet chemical method. Mater. Res. Bull. 48, 2878–2885. https://doi.org/10.1016/j.materresbull.2013.04.008.

Siemons, M., Leifert, A., Simon, U., 2007. Preparation and Gas Sensing Characteristics of Nanoparticulate p-Type Semiconducting LnFeO 3 and LnCrO 3 Materials. Adv. Funct. Mater. 17 (13), 2189–2197.

Soltani, T., Entezari, M.H., 2013. Solar photocatalytic degradation of RB5 by ferrite bismuth nanoparticles synthesized via ultrasound. Ultrason. Sonochem. 20, 1245–1253. https://doi.org/10.1016/j.ultsonch.2013.01.012.

Thommes, M., 2010. Physical Adsorption Characterization of Nanoporous Materials. Chemie Ingenieur Technik 82 (7), 1059–1073.

Waghmare, S.D., Jadhav, V.V., Shaikh, S.F., Mane, R.S., Rhee, J.H., O'Dwyer, C., 2018. Sprayed tungsten-doped and undoped bismuth ferrite nanostructured films for reducing and oxidizing gas sensor applications. Sensors Actuators, A Phys. 271. https://doi.org/10.1016/j.sna.2018.01.008.

Wang, J., Neaton, J.B., Zheng, H., Nagarajan, V., Ogale, S.B., Liu, B., Viehland, D., Vaithyanathan, V., Schlom, D.G., Waghmare, U.V., Spaldin, N.A., Rabe, K.M., Wuttig, M., Ramesh, R., 2003. Epitaxial BiFeO3 Multiferroic Thin Film Heterostructures. Science (80-.) 299, 1719–1722. https://doi.org/10.1126/science.1080615.

Wang, Y., Xu, G., Yang, L., Ren, Z., Wei, X., Weng, W., Du, P., Shen, G., Han, G., 2009. Hydrothermal synthesis of single-crystal bismuth ferrite nanoflakes assisted by potassium nitrate. Ceram. Int. 35, 1285–1287. https://doi.org/10.1016/j.ceramint.2008.04.016.

Yu, X.-L., Wang, Y., Hu, Y.-M., Cao, C.-B., Chan, H.L.-W., 2009. Gas-Sensing Properties of Perovskite BiFeO3 Nanoparticles. J. Am. Ceram. Soc. 92, 3105–3107. https://doi.org/10.1111/j.1551-2916.2009.03325.x.

Zhang, D., Liu, A., Chang, H., Xia, B., 2015. Room-temperature high-performance acetone gas sensor based on hydrothermal synthesized SnO2-reduced graphene oxide hybrid composite. RSC Adv. 5, 3016.

Zhang, J.X., Li, Y.L., Wang, Y., Liu, Z.K., Chen, L.Q., Chu, Y.H., Zavaliche, F., Ramesh, R., 2007. Effect of substrate-induced strains on the spontaneous polarization of epitaxial BiFeO3 thin films. J. Appl. Phys. 101. https://doi.org/10.1063/1.2743733.

Zhang, Y., Xu, H., Dong, S., Han, R., Liu, X., Wang, Y., Li, S., Bu, Q., Li, X., Xiang, J., 2018. A fast response & recovery acetone gas sensor based on BiFeO3 nanomaterials with high sensitivity and low detection limit. J. Mater. Sci. Mater. Electron. 29, 2193–2200. https://doi.org/10.1007/s10854-017-8132-7.

Zhu, K.M., Ma, S.Y., Pei, S.T., Tie, Y., Zhang, Q.X., Wang, W.Q., Xu, X.L., 2019. Preparation, characterizaton and formaldehyde gas sensing properties of walnut-shaped BiFeO3 microspheres. Mater. Lett. 246, 107–110. https://doi.org/10.1016/j.matlet.2019.02.129.